ADVANCED FUNCTIONAL MATERIALS
www.afm-journal.de

Formation of Bi_2WO_6 Bipyramids with Vacancy Pairs for Enhanced Solar-Driven Photoactivity

Gong Zhang, Ziyu Hu, Meng Sun, Yang Liu, Limin Liu, Huijuan Liu, Chin-Pao Huang, Jiuhui Qu, and Jinghong Li**

In order to improve the photoactivity, many attempts have focused on increasing the exposure of highly reactive surfaces on crystals. However, the connection between the reactive surfaces and enhancement is still elusive. Herein, Bi_2WO_6 nanostructured bipyramids with a large fraction of {100} facets are fabricated by the solvothermal method. The formation of "Bi–O" dimer vacancy pairs on the {100} high-energy facets is responsible for the reduction in band gap and the decrease in the recombination of photo-excited charge carriers, which is unambiguously confirmed by the positron annihilation spectra (PAS), X-ray photoelectron spectrum (XPS), and theoretical calculations. The effective separation of electron–hole pairs and the narrowing bandgap significantly improve the photoactivity of Bi_2WO_6 nanobipyramids, especially under solar light irradiation. These findings can be applied broadly to the design and fabrication of energy efficient and robust catalysts.

1. Introduction

Both energy and the environment are vital topics for human survival. Heterogeneous photocatalysts offer great potential for converting solar energy into chemical energy and for the environmental remediation.[1–5] Typical examples are TiO_2-based photocatalytic decomposition of organic contaminants and water-splitting. Plenty attempts have been made on modifying of the physical structure of TiO_2 crystals to enhancing its photoactivity.[6,7] TiO_2 has a wide bandgap of 3.2 eV, leading to only utilization of the UV region in solar resource, which limits its wide applications.[8–10] Therefore, the development of efficient solar-photoactive catalysts has become an active pursuit by many researchers aiming at harvesting solar energy effectively. Bismuth tungstate (Bi_2WO_6), stable, nontoxic, and with a relatively small bandgap of 2.6 eV has been suggested an ideal photocatalyst for applications in visible-light-driven photocatalysis.[11–15] To enhance the separation efficiency of the photoexcited charge carriers in Bi_2WO_6, great efforts have been made by adjusting the chemical composition or manipulating the physical structure.[16–20] There have studies on improving photoefficiency by chemical modification such as by partially substituting the M sites in the $A_xM_yO_z$ structure with alkalis or earth alkalis.[21–23] However, these ions tend to decrease the thermal stability and increase the recombination of charge centers of Bi_2WO_6.[24]

Therefore, modifying the physical morphology, to achieve more high energy surfaces in Bi_2WO_6, becomes an important alternative strategy for enhancing its photoactivity.[25] By exposing high-energy surfaces can enhance the photoelectric and photocatalytic properties of a catalyst.[26–29] Specifically, by increasingly exposing the high-energy facets in Bi_2WO_6 can improve the effective separation of electron–hole pairs, thereby arriving at the fabrication of more efficient catalysts. Moreover, to deduce the relationship between the ratio of high energy surface and the enhanced effect, the overwhelming majority of researchers have only fixed their attention on the strength of the interaction of the reactive surfaces with reactant molecules.[30] However, this explanation does not fully explain the enhancement. Recently, there are reports that these reactive facets are accompanied always by various types of surface defects.[31–33] Furthermore, with recent advances in scanning tunneling microscopy (STM), electron paramagnetic resonance spectroscopy (EPR), and positron annihilation spectroscopy (PAS),[34–36] the role of defects in photocatalysis now can be thoroughly studied. In contrast to bulk defects, which only act as trap sites for charge carriers, surface defects can be adsorption sites where charge carriers can be transferred more easily to the adsorbed species, thereby impeding their recombination and enhancing the photoefficiency. Therefore, it is hypothesized that surface defects on the reactive surfaces of a crystal can play an important role in controlling the photocatalytic efficiency.

G. Zhang, Dr. M. Sun, Prof. H. J. Liu, Prof. J. H. Qu
Key Laboratory of Drinking Water Science and Technology
Research Center for Eco-Environmental Sciences
Chinese Academy of Sciences
Beijing 100085, China
E-mail: hjliu@rcees.ac.cn

G. Zhang, Dr. M. Sun
University of Chinese Academy of Sciences
Beijing 100039, China

Dr. Z. Y. Hu, Prof. L. M. Liu
Beijing Computational Science Research Center
Beijing 100084, China

Dr. Y. Liu, Prof. J. H. Li
Department of Chemistry
Beijing Key Laboratory for Microanalytical Methods and Instrumentation
Tsinghua University
Beijing 100084, China
E-mail: jhli@mail.tsinghua.edu.cn

Prof. C.-P. Huang
Department of Civil and Environmental Engineering
University of Delaware, Newark
DE 19716, USA

DOI: 10.1002/adfm.201501009

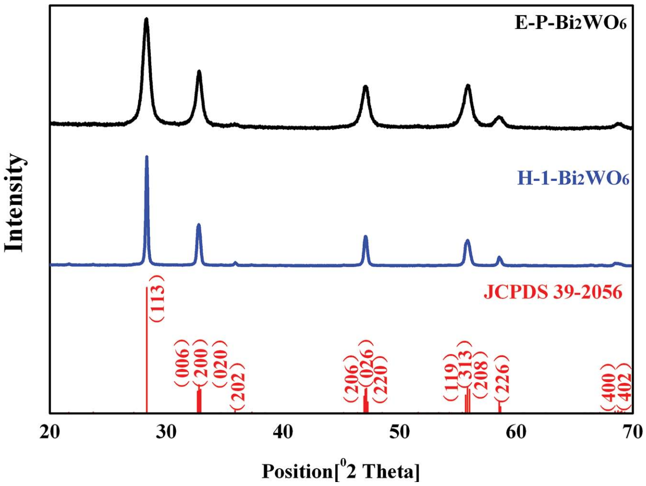

Figure 1. XRD spectra of plate-structure Bi_2WO_6 (P-Bi_2WO_6) (hydrothermal synthesis, pH = 1) and bipyramid-structured Bi_2WO_6 (B-Bi_2WO_6) (solvothermal synthesis, with PVP).

Herein, a facile procedure was used to fabricate Bi_2WO_6 nanobipyramids that have high density of high-energy facets. The photoelectric and photocatalytic characteristics of this Bi_2WO_6 nanobipyramids will be more photosensitive than those Bi_2WO_6 plates. In addition, the defects in the bipyramid-structured Bi_2WO_6 were characterized thoroughly by various surface and crystal chemistry techniques and verified by theoretical computations such as density of states and density function theory, as well as experimental techniques such as electrochemical impedance spectroscopy (EIS) and UV–vis light spectrophotometry as to gain insights into the effect of defects on photocatalytic properties.

2. Result and Discussion

The X-ray powder diffraction (XRD) patterns of the Bi_2WO_6 samples are shown in **Figure 1**. The peaks can clearly identify the orthorhombic phase of Bi_2WO_6 (JCPDS 39-0256). However, it is worth noting that obvious changes in the intensity ratios for various peaks can be observed. More specifically, in the case of plate-structured Bi_2WO_6 (P-Bi_2WO_6), the intensity ratio of the {200} to {113} facet was 0.3, which was remarkably smaller than 0.6 of bipyramid-structured Bi_2WO_6 (B-Bi_2WO_6). This indicated that B-Bi_2WO_6 with a larger fraction of {100} crystalline planes was fabricated successfully.

The morphologies of Bi_2WO_6 samples were characterized by FESEM. The products from the hydrothermal synthesis appear as 2D plates, and their morphologies were significantly affected by the pH conditions. When the pH was 1.0, the Bi_2WO_6 appeared of peony-like aggregations convoluted by lots of 2D nanoplates, which are denoted as P-Bi_2WO_6 (**Figure 2**a). As pH increased, the flower structure was disaggregated due to the anisotropic growth of the Bi_2WO_6 nanoplates (Figure S1b–d, Supporting Information). In the process of solvothermal synthesis, the polyvinylpyrrolidone (PVP) was utilized for modifying the morphology. Bipyramid-structured Bi_2WO_6 could be obtained in the presence of PVP (Figure 2c), while irregular Bi_2WO_6 nanoparticles were formed without PVP (Figure S2, Supporting Information). This is ascribed to the selective interactions between the PVP molecules and the specific planes of the Bi_2WO_6, which could significantly inhibit the anisotropic growth of {113} facets.[37–39] During the nucleation process, the "—C=O" in the PVP unit prefers to interact with the unsaturated atoms in order to reduce surface energy.[40] Therefore, the unsaturated "W" atoms on the Bi_2WO_6 surface are more active for bonding with PVP.[41] Thus, with the shrinkage

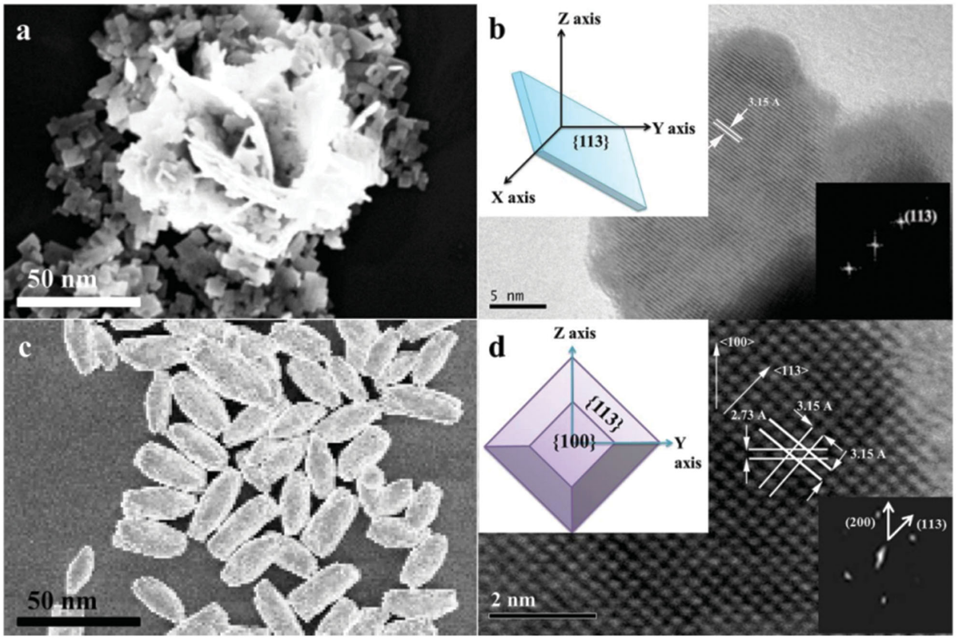

Figure 2. a) SEM and b) HRTEM images of the P-Bi_2WO_6 (hydrothermal synthesis, pH = 1); c) SEM and d) HRTEM images of the B-Bi_2WO_6 (solvothermal synthesis, with PVP) (inset showing their fast-Fourier transform patterns and the corresponding schematic drawings).

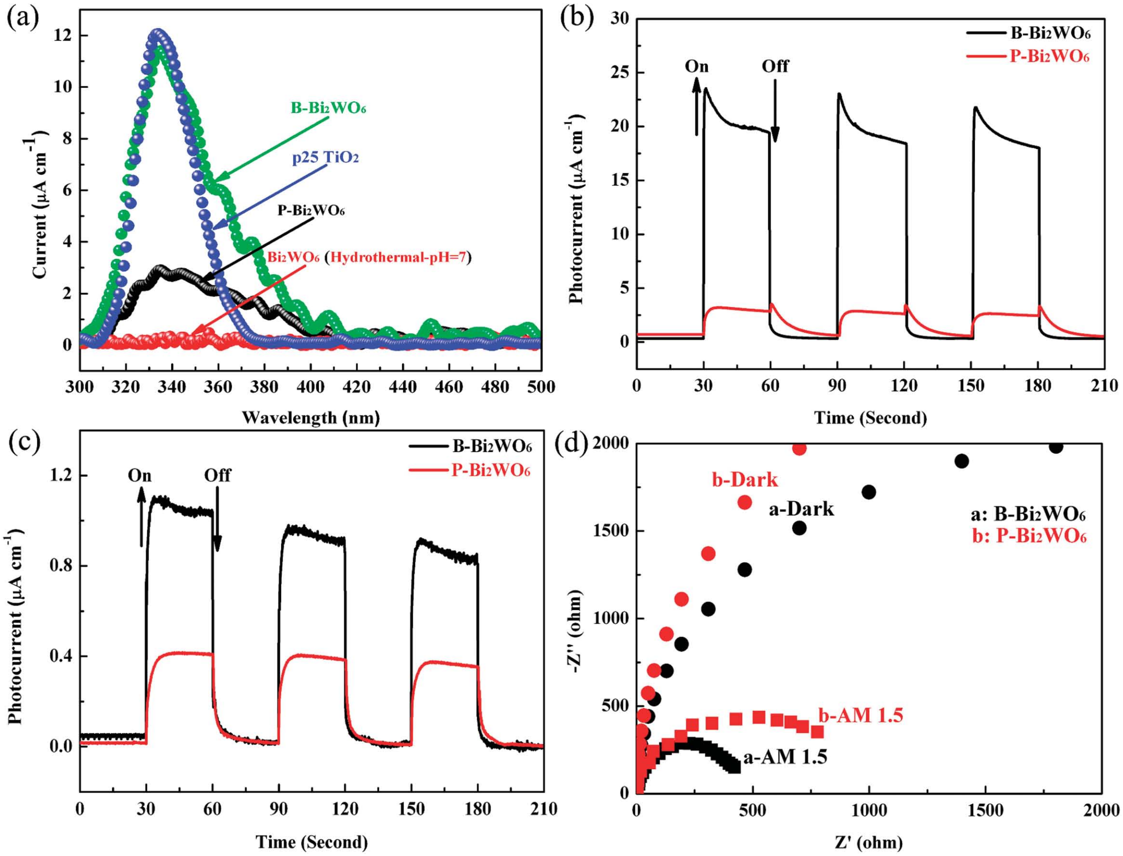

Figure 3. Photoelectrochemical properties of the two types of Bi_2WO_6: a) photocurrent action spectra under UV and visible light; chronoamperometry under b) solar light and c) visible light irradiation; d) the Nyquist plot of electrochemical impedance spectroscopy.

of the restricted planes and continuous enlargement of the other planes, a bipyramid structure evolved. Furthermore, the HRTEM image revealed also the crystalline details of Bi_2WO_6. In the P-Bi_2WO_6 crystal, the spacing at the lattice fringes was found to be 3.15 Å, which was corresponding to the {113} plane (Figure 2b) and was the most stable facet in Bi_2WO_6.[14] In addition, a truncated bipyramid of a B-Bi_2WO_6 nanocrystal was carefully analyzed by the HRTEM. The fringe spacing of 3.15 Å corresponds to {113} planes, while the spacing of 2.73 Å corresponds to {200} planes (Figure 2d). The above fringe spacing and the angle in the fast-Fourier transform (FFT) image (Figure 2d, inset) implied that the top/bottom surfaces of the truncation are bound by a (100) facet. The inset in Figure 2b,d shows sketched crystal structures of the P-Bi_2WO_6 and B-Bi_2WO_6, respectively.

Furthermore, the photoelectrochemical properties of the two types of Bi_2WO_6 were investigated. First, the conversion activity of photons to current was measured via photocurrent action spectra. Generally, higher photocurrent corresponds to higher separation efficiency for the photogenerated electron–hole pairs, and thus represents higher photoactivity.[42,43] **Figure 3**a shows the photoactivity of different Bi_2WO_6 photocatalysts including P25 TiO_2 for the purpose of comparison. Results clearly show that the plated-structured Bi_2WO_6 has a lower photocurrent property in the region from 300 to 360 nm in contrast to P25 TiO_2. However, as the morphology converted to bipyramid, the B-Bi_2WO_6 with an extensive number of {100} facet achieved much higher photocurrent efficiency than that of P-Bi_2WO_6. The maximum photocurrent of B-Bi_2WO_6 approximated to that of P25 TiO_2 in the region from 335 to 345 nm. Furthermore, in the region from 345 to 420 nm, even in visible light region (>420 nm), higher photocurrent was achieved in B-Bi_2WO_6, which could be benefit to the efficient utilization of the solar-light resource.

In addition, the effect of morphology on the photoresponse of Bi_2WO_6 was evaluated using chronoampermetric technique at +0.3 V. Upon power excitation, both types of Bi_2WO_6 displayed instantaneous photocurrent, which was then promptly returned to a steady state when the light was turned off. Notably, the bipyramid-structured B-Bi_2WO_6 showed a photocurrent density of 24 μA cm^{-2}, almost ten times that of the plate-structured P-Bi_2WO_6 (Figure 3b) under solar light irradiation. A similar trend was also observed under visible-light irradiation, except that the peak photocurrent was much smaller than that under solar light for both Bi_2WO_6 samples (Figure 3c). It is proposed that when the Bi_2WO_6 crystal containing more {100} facets will benefit the separation of photogenerated charge carriers. Figure 3d shows the Nyquist plot of results of electrochemical impedance spectroscopy (EIS) for both Bi_2WO_6 electrodes in dark and under light illumination. Results showed that the electrical resistance of both photocatalysts was smaller under light irradiation than that in dark as indicated by the

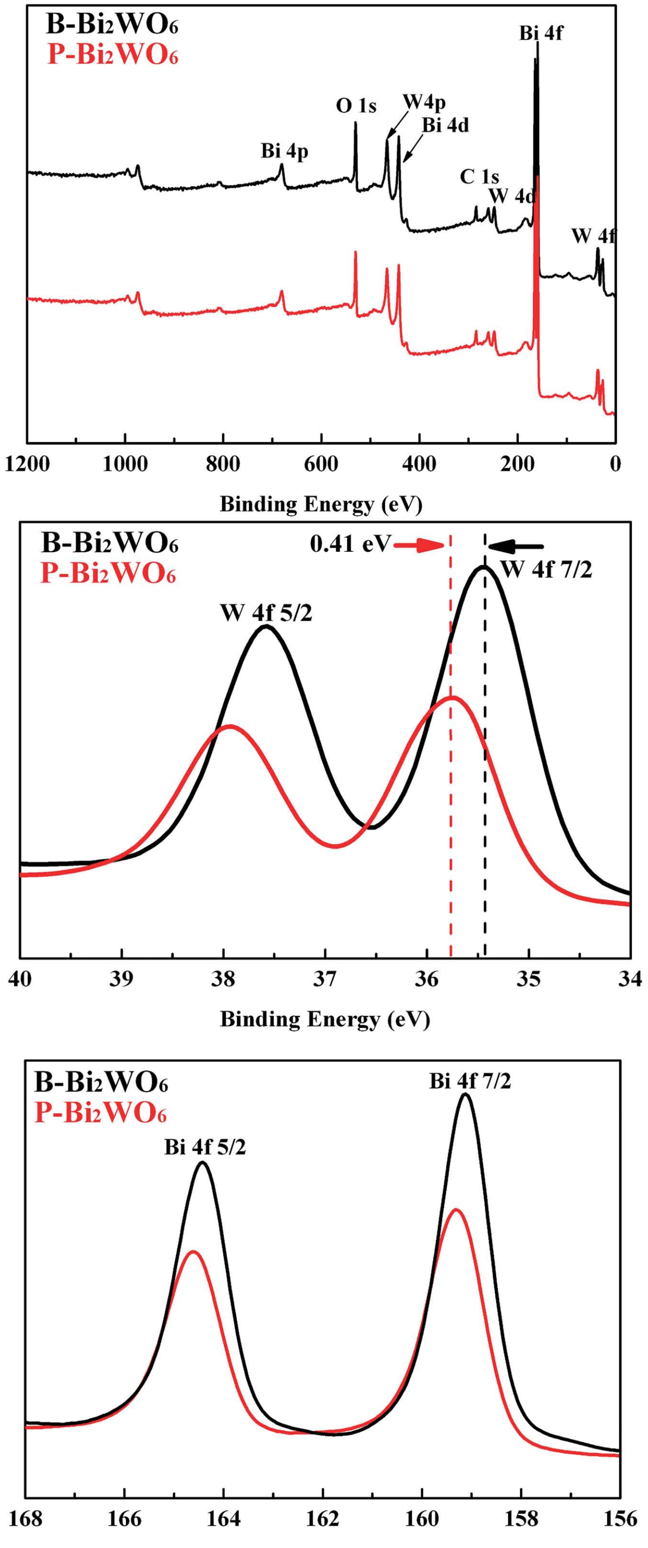

Figure 4. X-ray photoelectron spectra: full scan, W 4f, and Bi 4f regions of B-Bi_2WO_6 (solvothermal synthesis, with PVP) and P-Bi_2WO_6 (hydrothermal synthesis, pH = 1).

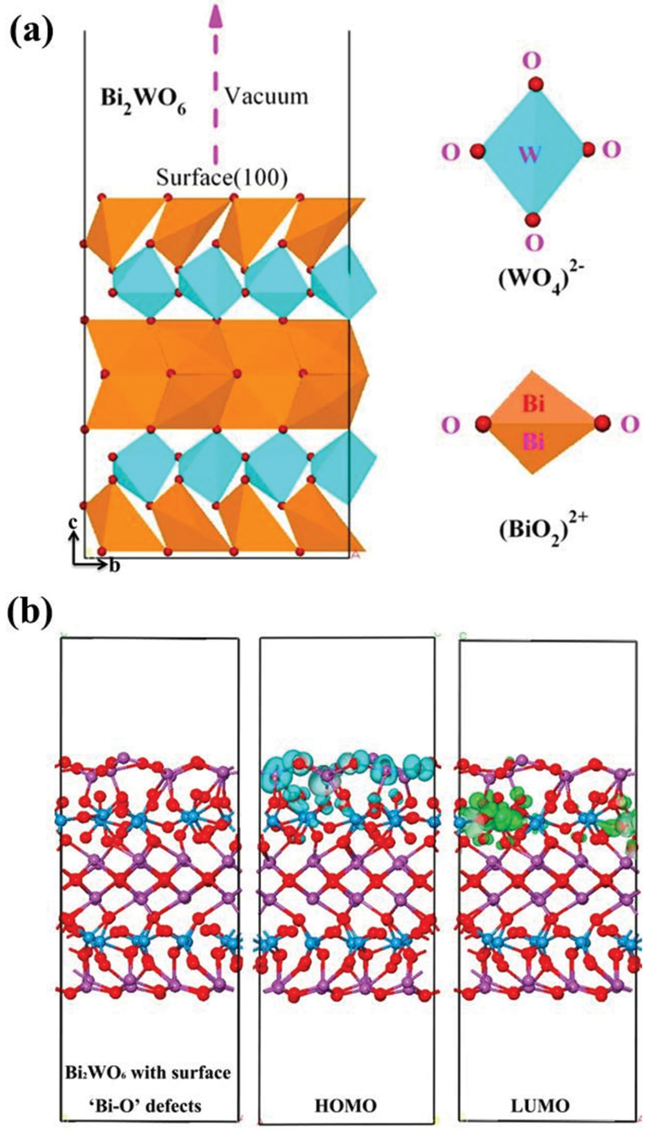

Figure 5. a) Schematic representation of the crystal structure of Bi_2WO_6. b) The optimized model of Bi_2WO_6 with surface defects (left). The electron density contour map for the top of the valence band (HOMO) (middle), and for the bottom of the conduction band (LUMO) (right). Purple, blue, and red balls represent Bi, W, and O atoms, respectively.

smaller semicircle of the Nyquist plot. Furthermore, in contrast to the P-Bi_2WO_6, the bipyramid-structured B-Bi_2WO_6 exhibited much smaller electrical resistance both in dark and under light irradiation, indicating that the structure facilitated charge transfer.

To clarify the underlying mechanism of the higher photoactivity for the Bi_2WO_6 bipyramids relative to plates, a density function theory (DFT) was performed to calculate the surface energy of the {100} and {113} facets of Bi_2WO_6. The calculation results show that the surface energy of the {100} facet (1.21 J m^{-2}) is higher than that of the {113} facet (1.02 J m^{-2}), implying that {100} facets should be more reactive than {113} facets. Generally, during the nucleation process of the catalysts, in order to maintain these surfaces with the high energy as much as possible, there occurs large-scale atom reconstruction on those facets, which leads to the formation of defects, accordingly.[44,45] Therefore, it is speculated that the Bi_2WO_6 with a

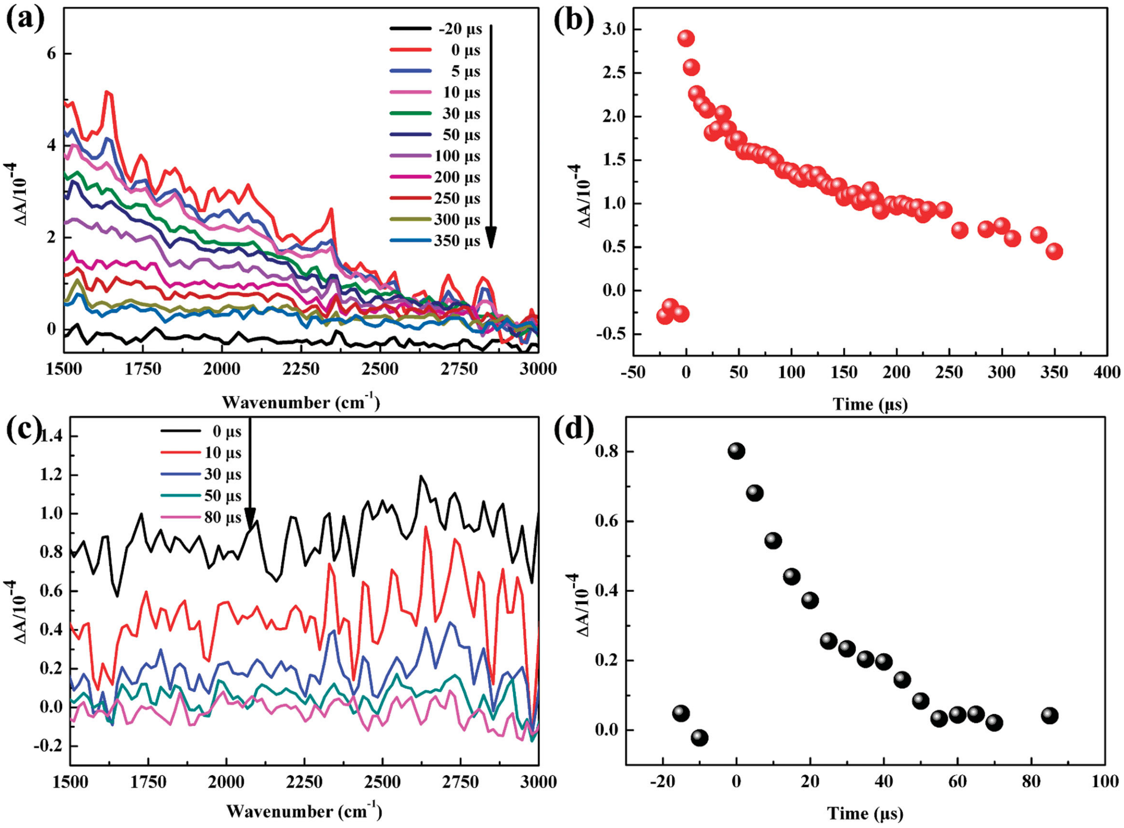

Figure 6. Transient IR absorption spectra of a) B-Bi_2WO_6 (solvothermal synthesis, with PVP) and c) P-Bi_2WO_6 (hydrothermal synthesis, pH = 1); time profiles of absorbance at 2000 cm^{-1} of b) B-Bi_2WO_6 and d) P-Bi_2WO_6 irradiated by 355 nm pulses in vacuum.

greater proportion of {100} facets would possess more surface defects, which serve as the major sites that increase the transfer of photoexcited charge carries.

The presence of defects was further verified by the positron annihilation measurements. **Table 1** shows the three positron lifetime components, τ_1, τ_2, and τ_3, with intensities I_1, I_2, and I_3. T_3 is due to the annihilation of orthopositronium atoms formed in the large voids present in the material.[46,47] T_1 generally results from the small-size defects that exist in the bulk.[48,49] T_2 derives from the positrons trapped by the larger size defects, which are mainly located on the surface of the materials.[50] The relative intensity (I) reflects the concentrations of the corresponding defects.[51] Results showed that the I_1/I_2 ratio was 0.6 and 1.22 for B-Bi_2WO_6 and P-Bi_2WO_6, respectively, indicating a higher concentration of surface defects in the B-Bi_2WO_6. In order to further identify the species making up the surface defects in B-Bi_2WO_6, the XPS measurements were performed to reveal the electronic structure of the two types of Bi_2WO_6. As depicted in **Figure 4**, the two Bi_2WO_6 samples are composed of four elements, Bi, O, W, and adventitious carbon. Besides, based on quantitative results areas, the atomic ratio of Bi and W in P-Bi_2WO_6 surface is calculated to be 2 ± 0.02:1, while the value is 1.9 ± 0.01:1 in B-Bi_2WO_6. In comparison with P-Bi_2WO_6, the peak of W 4f7/2 in B-Bi_2WO_6 shifted from 35.83 to 35.42 eV, indicating the variation of the electron density close to the W atoms due to the deficiency of Bi on the surface.[52–54] Meanwhile, according to the results of DFT calculations, the similar electronic environment appeared upon the introduction of "Bi-O" vacancy pairs on the {100} facet. Therefore, we speculated that the "Bi–O" dimer vacancy should be the most likely defect on the {100} facet in B-Bi_2WO_6.

Question arises, how the "Bi–O" vacancies affect the photoactivity of Bi_2WO_6? **Figure 5**a depicts the structure of a perfect Bi_2WO_6 {100} facet, which is constructed of perovskite-like $(WO_4)^{2-}$ and alternating $(Bi_2O_2)^{2+}$ units. Interestingly, after the introduction of dimer "Bi–O" vacancy pairs, the structure of the optimized model of the defect Bi_2WO_6 appears seriously distorted (Figure 5b), which can provide a larger space for polarizing the related atoms and orbitals, improving the separation efficiency of the electron–hole pairs.[55,56] To further verify the hypothesis, the transient infrared absorption for the two Bi_2WO_6 samples was subsequently measured. The transient infrared technique has been extensively used to study photocatalysts for understanding the optical transition of the photoelectron pairs in the conduction band. And the absorbance intensity at 2000 cm^{-1} of the time-resolved infrared

Table 1. Positron lifetime parameters of the P-Bi_2WO_6 plates and B-Bi_2WO_6 nanoparticles, respectively.

Sample	τ_1 [ps]	τ_2 [ps]	τ_3 [ns]	I_1 [%]	I_2 [%]	I_3 [%]	I_1/I_2
P-Bi_2WO_6	190.4	463	2.486	54.21	44.53	1.26	1.22
B-Bi_2WO_6	184.1	402	2.426	37.05	61.41	1.54	0.60

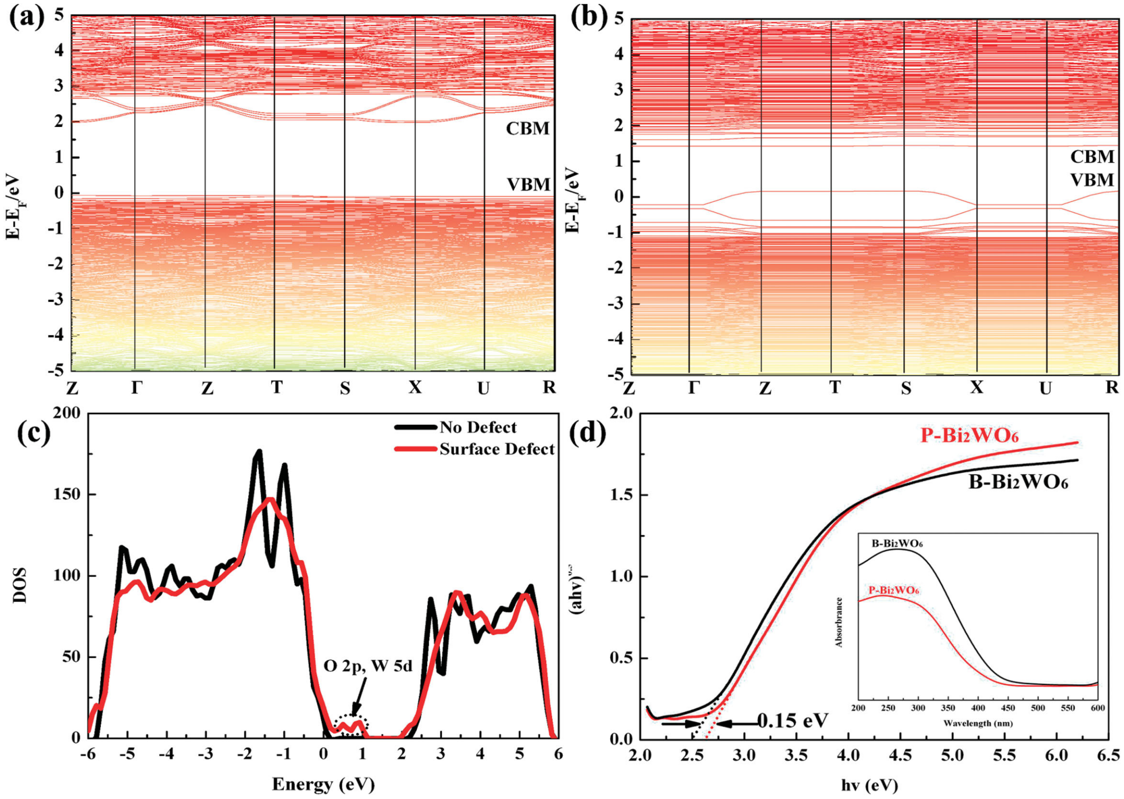

Figure 7. The calculated band structures of a) perfect Bi_2WO_6 and b) Bi_2WO_6 with surface defects; c) DOS diagram for Bi_2WO_6 with or without surface defect; d) the diffuse reflection spectra and Tauc plot of the two types of Bi_2WO_6.

absorption spectroscopy (TAS) reflects the quantity of photoexcited electrons, while the decay is due to their recombination with holes.[12,57] As shown in **Figure 6**a,c, at the onset of a laser pulse, there were rapid rises of the absorption peaks observed in both B-Bi_2WO_6 and P-Bi_2WO_6. It was also noted that there was much stronger intensity of the IR absorption or higher concentration of photoexcited electrons generated on B-Bi_2WO_6 surface.[58] The absorbance was barely measurable at 80 μs in P-Bi_2WO_6, whereas there was still considerable absorbance intensity observed at 350 μs in B-Bi_2WO_6, which signifies a lower recombination of the electron–hole pairs (Figure 6b,d). Results clearly indicated that both the quantity (concentration) and the quality (lifetime) of photoelectrons on B-Bi_2WO_6 were significantly greater than on P-Bi_2WO_6, which is in close agreement with results of DFT calculations.

In addition, the density of states (DOS) of Bi_2WO_6 was studied. For perfect Bi_2WO_6 crystal, the valence band is composed of O 2p+Bi 6s6p, and the conduction band is contributed mainly from the O 2p+W 5d orbitals and to a lesser from the Bi 6p orbital (**Figure 7**a). According to the electron density contour maps for the bottom of the conduction band (LUMO), the existence of the "Bi–O" vacancy pairs causes the electron density to shift to W atoms (Figure 5b), and thereby changes the electronic structure of Bi_2WO_6. The change of the electronic structure results in a downshift of O 2p and W 5d orbitals to the VBM, and an upshift of Bi 6s6p orbitals to the CBM, which decrease the band gap energy of Bi_2WO_6 accordingly (Figure 7b,c). The above conclusion agrees with the results of diffuse reflection spectra (DRS) (Figure 7d). Results in Figure 7d showed that P-Bi_2WO_6 and B-Bi_2WO_6 had a band gap of or 2.65 and 2.50 eV, respectively. Therefore, it is believed that the maximum utilization of sunlight can be achieved in B-Bi_2WO_6.

Moreover, the photocatalytic performances of as-prepared Bi_2WO_6 samples have been estimated using DIC as the probe molecule. The DIC was chosen for two main reasons: (i) it exhibits no visible light absorption, excluding the effect of photosensitization during the photocatalytic process; (ii) the DIC has been detected in wastewater and drinking water,[59] which has toxicity to the liver, kidney, and gill cells, as well as causing renal lesions.[59–61] Therefore, it is of great significance to remove DIC from aqueous systems. In the presence of B-Bi_2WO_6, nearly 30 ± 5% of DIC is adsorbed in dark. Under solar light irradiation, the degradation of DIC followed a pseudo-first-order kinetics with an apparent rate constant (*k*) of 3.127 min^{-1} by B-Bi_2WO_6, which was almost ten and three times higher than that by P-Bi_2WO_6 and P25 TiO_2, respectively (**Figure 8**a). With exposure to visible light (>420 nm), in contrast to the negligence effect with P25 TiO_2 (Figure S4, Supporting Information), the photocatalytic degradation of DIC by B-Bi_2WO_6 was completed in 30 min (Figure 8c). The outstanding photocatalytic performances essentially in agreement with the results of the above photoelectrochemical measurements, and this confirmed the B-Bi_2WO_6 had unlimited potential in the application of the solar light. Furthermore, it is worthy of notice that the quadruple time-of-flight mass spectrometry (Q-TOF-MS) signal of B-Bi_2WO_6 treated DIC

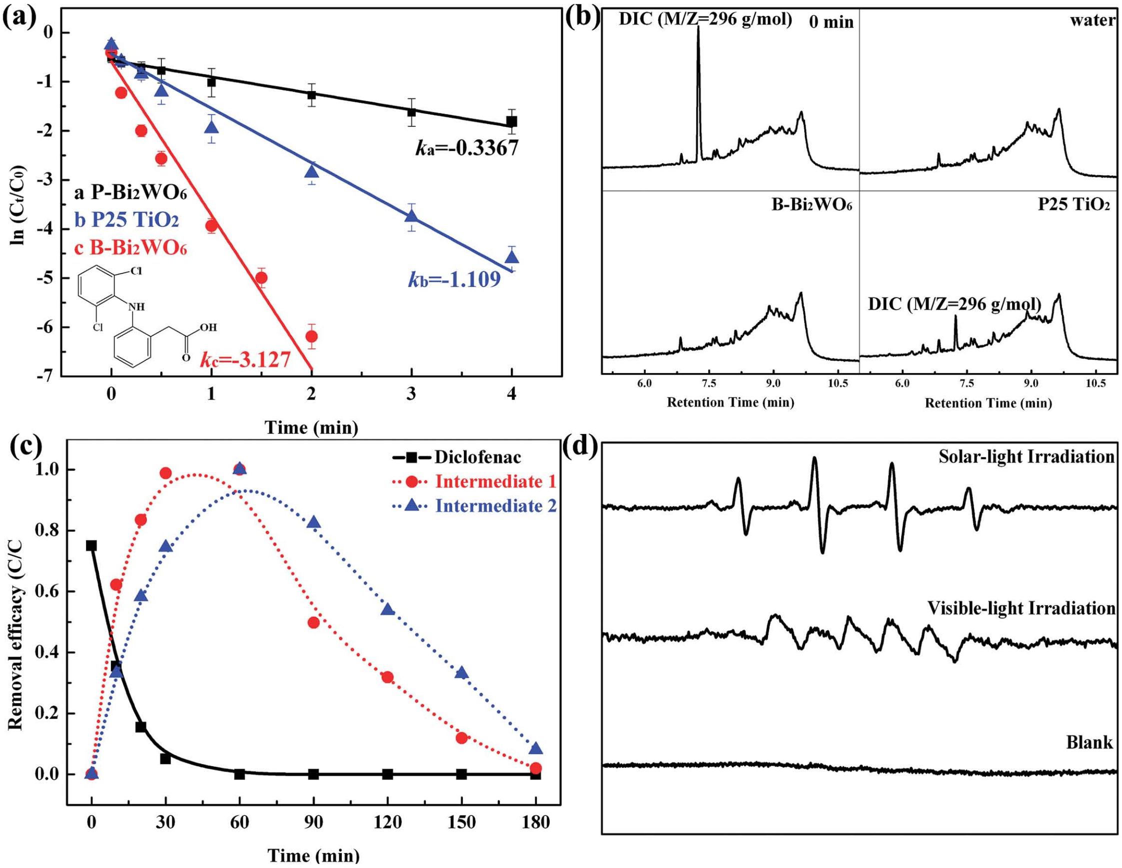

Figure 8. a) Photocatalytic degradation of DIC in the presence of different catalysts under solar light irradiation. b) Q-TOF-MS results of aqueous DIC, pure water, and the samples after 4 min reaction with B-Bi_2WO_6 and P 25 TiO_2 under solar light irradiation. c) Degradation of DIC in the presence of B-Bi_2WO_6 with visible light. d) EPR spectra of the DMPO —•OH adducts and —O^{2-}•/ HO^{-2}• recorded with B-Bi_2WO_6 under solar and visible light irradiation.

containing solution became identical to that of ultrapure water, whereas the TiO_2-treated DIC solution still showed the presence of numeral intermediates (Figure 8b).

ESR spectra and radical-trapping experiments were carried out for B-Bi_2WO_6. A fourfold characteristic peak with an intensity ratio of 1:2:2:1 was observed for DMPO-•OH adduct, as shown in Figure 8d. Under visible light, the sextet peak of DMPO-O^{2-}•/HO^2• adduct was observed. Therefore, it is reasonable to suggest that the reactive oxygen species (ROS) generated in the aqueous solution contributes to the high efficient photocatalytic performance. Additionally, the stability of the photocatalysts was studied by multicycle degradation experiments. The photoactivity of B-Bi_2WO_6 remained high and constant over ten consecutive cycles (Figure S7, Supporting Information), which indicates the stability of the photocatalyst. For practical application of photocatalysis to environmental remediation, it is especially important that the photocatalysts have high degree of stability.

3. Conclusion

Bi_2WO_6 nanobipyramid was fabricated via a facile strategy successfully. Results of theoretical calculations and experimental observations clearly showed that the presence of a high density of the high energy surface {100} in Bi_2WO_6 was important to the formation of defects, i.e., "Bi–O" vacancy pairs, which were keys to the increase in solar-light photoactivity. Accordingly, the presence of vacancy pairs changed the chemical and electronic structure of Bi_2WO_6, which, in turn, promoted the degree of the separation of the photogenerated electron–hole pairs, narrowed the band gap energy, and ultimately increased the utilization efficiency of the solar light. The nature of a nanobipyramid structure in Bi_2WO_6 can enhanced the photoactivity significantly. The findings provided insights into the mechanisms on photoactivity by elucidating the connection between reactive surfaces and enhanced photochemical reactivity; an information useful to the design and fabrication sensitive catalysts.

4. Experimental Section

Materials: All chemical reagents were purchased and used without further purification including bismuth nitrate (Aldrich), sodium tungstate (Alfa), polyvinylpyrrolidone (PVP) (M_w = 30 000, Aldrich), nitric acid (HNO_3) (guaranteed reagent), ethylene glycol (EG) (guaranteed reagent, 100%), diclofenac sodium (Sigma). TiO_2 particles (P25, Degussa) were purchased form Degussa Co.

Fabrication of Bismuth Tungstate: Bipyramid-structured Bi_2WO_6 (B-Bi_2WO_6). 1.2 g PVP was dissolved in 40 mL boiling ethylene glycol to gain a transparent mixture; then, 2 mmol $Bi(NO_3)_3$•$5H_2O$ was dissolved in the solution within 2 min. Finally, 1.0 mmol of Na_2WO_4•$2H_2O$ was added. After reaction 60 min under ultrasound, the mixture was transferred to a Teflon-lined autoclave (filled up to 80% of its total volume). The autoclave was sealed and maintained in an electro-oven at 180 °C for 24 h. After the autoclave was air-cooled to room temperature, the mixture was filtered, washed with distilled water and absolute alcohol several times to collect Bi_2WO_6, which was named B-Bi_2WO_6.

Plate-Structured Bi_2WO_6 (P-Bi_2WO_6): First, 2 mmol $Bi(NO_3)_3$•$5H_2O$ was dissolved in 15 mL 10% HNO_3 solution (Solution I). After stirring for 60 min, 15 mL of the aqueous solution containing 1.0 mmol of $Na_2WO_4 \cdot 2H_2O$ was added to solution I under continuous stirring. Then, the pH value of the resulting white suspension was adjusted to 1.0 with NaOH (4 M) solution. The obtained colloidal precipitate was transferred into a 40 mL Teflon lined autoclave. The colloidal precipitate was transferred to a 40 mL Teflon lined autoclave tube and autoclaved at 180 °C for 24 h, the Bi_2WO_6 so collected was denoted as P-Bi_2WO_6.

Characterizations: The crystal structure of samples was characterized by powder X-ray diffraction (XRD) (X'Pert Pro PW 3040-Pro, PANalytical, Inc.) using Cu Kα irradiation operating at 40 kV and 40 mA with a fixed slit. The morphologies of the samples were observed with a scanning electron microscope (SEM). The lattice and fringe spacings were obtained with a JEOL high-resolution transmission electron microscope (HRTEM). Specific surface area was measured by a volumetric method on an automatic adsorption instrument. XPS experiments were performed on Bi_2WO_6 with a PHI5000 Versa Probe system (Physical Electronics, MN), and the binding energies of XPS spectra were calibrated with the reference to the C1s peak at 284.80 eV. To investigate the light absorption and emission behavior, UV–vis absorption spectra were utilized in diffuse reflection mode using an integrating sphere (UV2401/2, Shimadzu). The characteristics of the photogenerated electrons were studied with time-resolved infrared absorption spectroscopy, and the light source for the photoexcitation was the third harmonic of a Q-switched Nd:YAG laser. The samples were fixed on a calcium fluoride (CaF_2) plate with a density of 1.5 mg cm^{-2}. The infrared (IR) light emitted from a $MoSi_2$ source was focused on the Bi_2WO_6 samples in vacu. The IR output was transformed to an electric signal in an MCT detector.

Photoelectrochemical Measurements: The photocurrent action spectra were measured in a home-built two-electrode configuration experimental system,[62] where the photocatalysts coated on ITO-coated glass by the doctor-blade method served as the working electrode, with an active area of 1 cm^{-2}, and a platinum wire was used as the counter electrode in the 0.2 M KCl electrolyte. A 500 W Xenon lamp with a monochromator was used as the light source. The cell was illuminated from the ITO side of the Bi_2WO_6 electrode by the incident light. The photocurrent signal was collected using a lock-in amplifier (Stanford Instruments SR830 DSP). The light intensity was 15 μW cm^{-2}, and the illumination area of the working electrode was 0.12 cm^{-2}. Before measurements, an experiment using a P25 TiO_2-coated electrode was performed as a reference. The photoelectrochemical properties in this study were measured using a Princeton Versa STAT 3 in a standard three-electrode configuration with Bi_2WO_6 electrodes used as photoanodes, Pt foil as the counter electrode, and an Ag/AgCl electrode as the reference electrode. 0.2 M KCl purged with N_2 was used as an electrolyte. An AM 1.5 solar power system was used as the light irradiation source.

Photocatalytic Test: A 300 W Xenon lamp was used as solar light, and wavelengths below 420 nm were cut off by an optical filter for visible light. The photocatalytic performance was evaluated by the degradation of Diclofenac (DIC) with initial concentration of 20 mg L^{-1}. More specifically, 50 mg catalyst samples were added to 100 mL of contaminant-containing solution. Before irradiation, to achieve adsorptive equilibrium, suspensions were mixed under vigorous stirring in the dark. After desired intervals, samples were taken and centrifuged to separate the supernatant liquid from catalysts. In addition, degradation test of the contaminant with P25 TiO_2 was used as control.

Positron Annihilation Measurement: Positron annihilation lifetime spectra (PALS) were measured using a conventional fast-slow coincident system. The coincidence spectrometer used had a prompt time resolution of 208 ps (FWHM) for the γ-rays from a 60Co source selected under the experimental conditions. The sample powders were pressed into a disk (diameter: 10.0 mm, thickness: 1.0 mm). A 30 μci 22Na positron source was sandwiched between two identical sample disks.

Supporting Information

Supporting Information is available from the Wiley Online Library or from the author.

Acknowledgements

This work was financially supported by the National Science Fund for Distinguished Young Scholars of China (Grant No. 51225805), the Funds for Creative Research Groups of China (No. 51221892), and National Basic Research Program of China (No. 2013CB934004). The authors thank the reviewers' very useful comments to enhance the paper quality.

Received: March 14, 2015
Revised: April 20, 2015
Published online: May 13, 2015

---

[1] W. Du, G. Yang, E. Wong, N. A. Deskins, A. I. Frenkel, D. Su, X. Teng, *J. Am. Chem. Soc.* **2014**, *136*, 10862.
[2] B. Oregan, M. Gratzel, *Nature* **1991**, *353*, 737.
[3] Z. Cui, H. Chen, M. Zhao, D. Marshall, Y. Yu, H. Abruna, F. J. DiSalvo, *J. Am. Chem. Soc.* **2014**, *136*, 10206.
[4] W. Zhou, W. Li, J. Q. Wang, Y. Qu, Y. Yang, Y. Xie, K. Zhang, L. Wang, H. Fu, D. Zhao, *J. Am. Chem. Soc.* **2014**, *136*, 9280.
[5] X. Gao, H. B. Wu, L. Zheng, Y. Zhong, Y. Hu, X. W. Lou, *Angew. Chem. Int. Ed.* **2014**, *53*, 5917.
[6] B. Liu, H. M. Chen, C. Liu, S. C. Andrews, C. Hahn, P. Yang, *J. Am. Chem. Soc.* **2013**, *135*, 9995.
[7] S. Liu, J. Yu, M. Jaroniec, *Chem. Mat.* **2011**, *23*, 4085.
[8] S. U. M. Khan, M. Al-Shahry, W. B. Ingler, *Science* **2002**, *297*, 2243.
[9] S. Livraghi, M. C. Paganini, E. Giamello, A. Selloni, C. Di Valentin, G. Pacchioni, *J. Am. Chem. Soc.* **2006**, *128*, 15666.
[10] J. Wang, D. N. Tafen, J. P. Lewis, Z. Hong, A. Manivannan, M. Zhi, M. Li, N. Wu, *J. Am. Chem. Soc.* **2009**, *131*, 12290.
[11] A. Kudo, S. Hijii, *Chem. Lett.* **1999**, *10*, 1103.
[12] F. Amano, A. Yamakata, K. Nogami, M. Osawa, B. Ohtani, *J. Am. Chem. Soc.* **2008**, *130*, 17650.
[13] H. Tong, S. Ouyang, Y. Bi, N. Umezawa, M. Oshikiri, J. Ye, *Adv. Mater.* **2012**, *24*, 229.
[14] C. Zhang, Y. F. Zhu, *Chem. Mat.* **2005**, *17*, 3537.
[15] L.-W. Zhang, Y.-J. Wang, H.-Y. Cheng, W.-Q. Yao, Y.-F. Zhu, *Adv. Mater.* **2009**, *21*, 1286.
[16] J. Yu, J. Low, W. Xiao, P. Zhou, M. Jaroniec, *J. Am. Chem. Soc.* **2014**, *136*, 8839.
[17] L. Etgar, P. Gao, Z. Xue, Q. Peng, A. K. Chandiran, B. Liu, M. K. Nazeeruddin, M. Graetzel, *J. Am. Chem. Soc.* **2012**, *134*, 17396.
[18] Y. Huang, E. J. Kramer, A. J. Heeger, G. C. Bazan, *Chem. Rev.* **2014**, *114*, 7006.
[19] L. Zhang, D. Bahnemann, *Chem. Sus. Chem.* **2013**, *6*, 283.
[20] L. Zhang, C. Baumanis, L. Robben, T. Kandiel, D. Bahnemann, *Small* **2011**, *7*, 2714.

[21] L. Zhang, Y. Man, Y. Zhu, *ACS Catal.* **2011**, *1*, 841.
[22] Z. G. Zou, J. H. Ye, K. Sayama, H. Arakawa, *Chem. Phys. Lett.* **2001**, *343*, 303.
[23] M. Yoshino, M. Kakihana, *Chem. Mat.* **2002**, *14*, 3369.
[24] X. Ding, K. Zhao, L. Zhang, *Environ. Sci. Technol.* **2014**, *48*, 5823.
[25] H. G. Yang, G. Liu, S. Z. Qiao, C. H. Sun, Y. G. Jin, S. C. Smith, J. Zou, H. M. Cheng, G. Q. Lu, *J. Am. Chem. Soc.* **2009**, *131*, 4078.
[26] H. G. Yang, C. H. Sun, S. Z. Qiao, J. Zou, G. Liu, S. C. Smith, H. M. Cheng, G. Q. Lu, *Nature* **2008**, *453*, 638.
[27] C. Li, C. Koenigsmann, W. Ding, B. Rudshteyn, K. R. Yang, K. P. Regan, S. J. Konezny, V. S. Batista, G. W. Brudvig, C. A. Schmuttenmaer, J. H. Kim, *J. Am. Chem. Soc.* **2015**, *137*, 1520.
[28] T. Tachikawa, S. Yamashita, T. Majima, *J. Am. Chem. Soc.* **2011**, *133*, 7197.
[29] R. Li, H. Han, F. Zhang, D. Wang, C. Li, *Environ. Sci. Technol.* **2014**, *7*, 1369.
[30] J. S. Chen, Y. L. Tan, C. M. Li, Y. L. Cheah, D. Luan, S. Madhavi, F. Y. C. Boey, L. A. Archer, X. W. Lou, *J. Am. Chem. Soc.* **2010**, *132*, 6124.
[31] F. Zuo, L. Wang, T. Wu, Z. Zhang, D. Borchardt, P. Feng, *J. Am. Chem. Soc.* **2010**, *132*, 11856.
[32] X. Zhang, L. Zhang, *J. Phys. Chem. C* **2010**, *114*, 18198.
[33] J. Zhuang, W. Dai, Q. Tian, Z. Li, L. Xie, J. Wang, P. Liu, X. Shi, D. Wang, *Langmuir* **2010**, *26*, 9686.
[34] Y. He, A. Tilocca, O. Dulub, A. Selloni, U. Diebold, *Nat. Mater.* **2009**, *8*, 585.
[35] J. Lee, D. C. Sorescu, X. Deng, *J. Am. Chem. Soc.* **2011**, *133*, 10066.
[36] T. Berger, M. Sterrer, O. Diwald, E. Knozinger, D. Panayotov, T. L. Thompson, J. T. Yates, *J. Phys. Chem. B* **2005**, *109*, 6061.
[37] Z.-m. Xiu, Q.-b. Zhang, H. L. Puppala, V. L. Colvin, P. J. J. Alvarez, *Nano Lett.* **2012**, *12*, 4271.
[38] D. Seo, J. C. Park, H. Song, *J. Am. Chem. Soc.* **2006**, *128*, 14863.
[39] Y. G. Sun, Y. N. Xia, *Science* **2002**, *298*, 2176.
[40] D. F. Zhang, H. Zhang, L. Guo, K. Zheng, X. D. Han, Z. Zhang, *J. Mater. Chem.* **2009**, *19*, 5220.
[41] D. G. Barton, S. L. Soled, G. D. Meitzner, G. A. Fuentes, E. Iglesia, *J. Catal.* **1999**, *181*, 57.
[42] M. Shao, F. Ning, M. Wei, D. G. Evans, X. Duan, *Adv. Funct. Mater.* **2014**, *24*, 580.
[43] R. Franking, L. Li, M. A. Lukowski, F. Meng, Y. Tan, R. J. Hamers, S. Jin, *Environ. Sci. Technol.* **2013**, *6*, 500.
[44] A. K. P. Mann, Z. Wu, F. C. Calaza, S. H. Overbury, *ACS Catal.* **2014**, *4*, 2437.
[45] Q. Q. Jia, H. M. Ji, D. H. Wang, X. Bai, X. H. Sun, Z. G. Jin, *J. Mater. Chem. A* **2014**, *2*, 13602.
[46] M. Kong, Y. Li, X. Chen, T. Tian, P. Fang, F. Zheng, X. Zhao, *J. Am. Chem. Soc.* **2011**, *133*, 16414.
[47] A. Sachdeva, S. V. Chavan, A. Goswami, A. K. Tyagi, P. K. Pujari, *J. Solid State Chem.* **2005**, *178*, 2062.
[48] S. Dutta, S. Chattopadhyay, D. Jana, A. Banerjee, S. Manik, S. K. Pradhan, M. Sutradhar, A. Sarkar, *J. Appl. Phys.* **2006**, *100*, 114328.
[49] H. Murakami, N. Onizuka, J. Sasaki, N. Thonghai, *J. Mater. Sci.* **1998**, *33*, 5811.
[50] X. Liu, K. Zhou, L. Wang, B. Wang, Y. Li, *J. Am. Chem. Soc.* **2009**, *131*, 3140.
[51] M. Guan, C. Xiao, J. Zhang, S. Fan, R. An, Q. Cheng, J. Xie, M. Zhou, B. Ye, Y. Xie, *J. Am. Chem. Soc.* **2013**, *135*, 10411.
[52] M. Wakisaka, S. Mitsui, Y. Hirose, K. Kawashima, H. Uchida, M. Watanabe, *J. Phys. Chem. B* **2006**, *110*, 23489.
[53] H. B. Liu, R. J. Hamers, *Surf. Sci.* **1998**, *416*, 354.
[54] P. Marcus, M. E. Bussell, *Appl. Surf. Sci.* **1992**, *59*, 7.
[55] J. Sato, N. Saito, H. Nishiyama, Y. Inoue, *J. Phys. Chem. B* **2003**, *107*, 7965.
[56] Z.-Y. Zhao, W.-W. Dai, *Inorg. Chem.* **2014**, *53*, 13001.
[57] A. Yamakata, T. Ishibashi, H. Onishi, *J. Phys. Chem. B* **2001**, *105*, 7258.
[58] T. Saison, P. Gras, N. Chemin, C. Chaneac, O. Durupthy, V. Brezova, C. Colbeau-Justin, J.-P. Jolivet, *J. Phys. Chem. C* **2013**, *117*, 22656.
[59] A. Kruglova, P. Ahlgren, N. Korhonen, P. Rantanen, A. Mikola, R. Vahala, *Sci. Total Environ.* **2014**, *499*, 394.
[60] L. A. Perez-Estrada, S. Malato, W. Gernjak, A. Aguera, E. M. Thurman, I. Ferrer, A. R. Fernandez-Alba, *Environ. Sci. Technol.* **2005**, *39*, 8300.
[61] J.-M. Kallio, M. Lahti, A. Oikari, L. Kronberg, *Environ. Sci. Technol.* **2010**, *44*, 7213.
[62] G. Wang, Q. Wang, W. Lu, J. Li, *J. Phys. Chem. B* **2006**, *110*, 22029.